HPU/sulfur nanoparticles decorated RGO nanocomposite as an antimicrobial smart material

Highlights

This chapter describes the preparation, characterization and property evaluation of HPU/sulfur nanoparticles decorated-reduced graphene oxide (HPU/SRGO) nanocomposite. This nanocomposite is studied here as an antimicrobial smart material. In this investigation, SRGO nanohybrid was prepared by a one-step eco-friendly strategy using the combined effect of the polyphenolic compounds and acids present in *Citrus limon* juice. The prepared nanohybrid and nanocomposite were characterized by different spectroscopic and analytical tools. The fabricated nanocomposite exhibited good thermal and mechanical properties as well as repeated self-healing ability and shape memory behavior under exposure of MW and direct sunlight. The nanocomposite also demonstrated profound microbial inhibitory effect against *Staphylococcus aureus*, *Escherichia coli* and *Candida albicans*. Thus, the studied nanocomposite demonstrates tremendous potential for various advanced applications.

Parts of this chapter are published in

Thakur, S., Das, G., Raul, P., Karak, K. Green one-step approach to prepare sulfur/reduced graphene oxide nanohybrid for effective mercury ions removal, *J. Phys. Chem. C* **117** (15), 7636--7642, 2013.

Thakur, S., Barua, S. Karak, N. Self-healable castor oil based tough smart hyperbranched polyurethane nanocomposite with antimicrobial attributes, *RSC Adv.* **5**, 2167--2176, 2015.

5.1. Introduction

The previous chapter addresses the development of HPU/IO-RGO nanocomposite as a multi-stimuli responsive repeated self-healing and shape memory materials with good mechanical properties. The fabricated nanocomposite exhibits tremendous potential in various applications such as smart coating, biomaterials, etc. However, microbial fouling is a vital issue for polymeric materials that causes degradation of them in course of service time.[1] Interestingly, vegetable oil based HPU exhibited biodegradability on exposure to different microbes.[2] Therefore, there is a huge chance for encountering of microbes and deteriorate the property of such smart materials during their service period. Even though, SHPs are capable to repair their damages, it requires time. Further, healing becomes tough under very harsh conditions. Again, the microbial problem is more pronounced in the bio-related application of such smart materials.[3] Hence, it needs proper attention to find out a suitable way to address such problems. Antimicrobial attributes in such polymer are designed to tackle the above-mentioned inconvenience.[4] In this regard, the antimicrobial potency of the nanomaterials are attained the copious attention of the scientific community.[5,6] After incorporation of such nanomaterial, the pristine polymer exhibits good antimicrobial attributes. In this context, graphene based materials such as GO, RGO demonstrate good antimicrobial activity against both gram positive and negative bacteria.[7,8] In addition, sulfur-containing compounds and polysulfanes show significant potential as antimicrobial agents.[9] Therefore, a sulfur nanoparticles-decorated RGO (SRGO) nanohybrid may show a synergistic effect and hence would be the right choice to prepare antimicrobial HPU nanocomposites.

A variety of methods are employed for the preparation of SRGO nanohybrid. These include, (i) sulfur nanoparticles can be precipitated on an aqueous suspension of RGO through a disproportionation reaction of thiosulfate solution in the presence of acid, (ii) sulfur nanoparticles can be dispersed in GO sheet followed by reduction of the GO using reducing agent such as hydrazine, and (iii) melted sulfur can also be deposited on RGO to prepare this nanohybrid.[10-12] However, these conventional methods are multistep process as well as environmentally hazardous, which limits their use. On the contrary, a single-step synthetic technique is in accordance to the tenets of green chemistry as it minimizes the energy, resources and time. Therefore, a greener and one step preparative technique is more appreciable for the simultaneous reduction of GO and formation of sulfur nanoparticles. It is reported that weak organic acids are more efficient to form finer sulfur nanoparticles by

disproportionation reaction of thiosulfate compared to inorganic strong acid.[13] In this context, lemon (*Citrus limon*) juice contains a high amount of weak organic acids such as citric and ascorbic acids which assist to the disproportionation reaction of thiosulfate.[14] In addition, the reduction of GO may be envisaged in parallel lines due to the combined effects of polyphenolic compounds as well as ascorbic acid, which abound in lemon juice, and thiosulfate in the reaction mixture. So, lemon juice is a good choice for achieving a double reward in the same pot.

Therefore, in the present study, SRGO nanohybrid was prepared by a greener one-pot technique using lemon juice as an acid source and an elastomeric HPU nanocomposite was fabricated using different wt% of the prepared nanohybrid. The prepared nanohybrid and fabricated nanocomposite were characterized by different spectroscopic and analytical tools. The mechanical properties, self-healing ability, shape memory behavior and antimicrobial properties of the nanocomposites were also explored.

5.2. Experimental

5.2.1. Materials

The same monoglyceride of the castor oil, TDI, PCL and BD were used for the preparation of HPU as described in Chapter 2, section 2.2.1. The same GO as reported in sub-chapter 3A was used for the preparation of SRGO nanohybrid.

Sodium thiosulfate pentahydrate ($Na_2S_2O_3.5H_2O$) was procured from Merck, India. Its molar mass, density and melting point are 248.18 g/mol, 1.667 g/cm^3 and 48.3 °C, respectively. It is widely used in the tanning of leather and pharmaceutical preparations as an anionic surfactant to aid in dispersion. Here, it was used as a precursor of sulfur nanoparticles.

Lemon (*C. limon*) was collected from Tezpur University campus. The juice of the lemon contains about 5-6% citric acid. It was the primary commercial source of citric acid before the development of fermentation-based processes. It is used as a cleaning agent, disinfectant, medicine, etc. Here, lemon juice was used as a weak acid source for formation of sulfur nanoparticles in the nanohybrid.

5.2.2. Characterization

FTIR, XRD, DSC and TGA analyses, and mechanical tests were performed under the same conditions and by using the same instruments as described in Chapter 2, section 2.2.2.

Raman spectra of SRGO nanohybrid were taken by the same Raman spectroscope and same condition as mentioned in sub-chapter 3A, section 3A.2.2. The morphology and SAED pattern of SRGO nanohybrid and HPU/SRGO nanocomposite were analyzed by same HRTEM as mentioned in sub-chapter 3A, section 3A.2.2. Shape memory test under MW and sunlight was performed by the same procedure as mentioned in the sub-chapter 3C, section 3C.2.2. Self-healing test was carried out under MW and sunlight using exactly similar method as mentioned in Chapter 4, section 4.2.2. The same domestic MW oven was used to test shape memory behavior and self-healing ability as mentioned in sub-chapter 3C, section 3C.2.2.

The antimicrobial activity of the nanomaterial and nanocomposite was tested against different microbial strains such as *Staphylococcus aureus* (ATCC 11632), *Escherichia coli* (ATCC 10536) and *Candida albicans* (ATCC 10231). Minimum inhibitory concentrations (MIC) were calculated for the nanomaterials and HPU, as well as for the nanocomposites. A micro-dilution technique was adopted for this assay.[15] *S. aureus* and *E. coli* were cultured in Nutrient Broth (NB, HiMedia, India) for 24 h at 37 °C. *C. albicans* was grown in Potato Dextrose Broth (PDB, HiMedia, India) for 48 h at 28 °C inside an incubator. A serial dilution was carried out for the samples (from stock solutions with concentration 30 mg mL^{-1}) using 1% dimethylsulfoxide (DMSO, HiMedia, India). Samples (100 mL) were incubated with the microbial cultures (100 mL) in 96 well plates at their specific concentrations. Streptomycin and nystatin (HiMedia, India) were taken as the positive controls. After incubation of 24 and 48 h, respectively, for bacteria and fungus, 40 mL of 3-(4,5-dimethylthiazol-2-yl)-2,5-diphenyltetrazolium bromide (MTT) was poured into each well. Change in color of the media to dark blue indicated the viable microbial cells, whereas no change in the color indicated the dead cells.

Further, microbial growth patterns were studied in the presence of HPU and the nanocomposite films. Microbial cultures were taken in 15 mL test tubes in the presence of the films and incubated for a specific time period. Growth was determined by recording their UV absorbance at 600 nm. Test tubes without film were considered as controls. Further, test tubes containing HPU were taken for comparative study. An SEM image was taken for *E. coli* as a representative species to observe the fate of the bacteria adhered to the films. Again, HPU and the nanocomposite films (1.5 cm x 1.5 cm x 0.3 mm) were laid on solidified agar plates, on which inoculums of bacteria and fungus were spread with the help of a spreader. These plates were incubated at 24 and 48 h at 37 and 28 °C in an incubator,

respectively. Microbial growth inhibition over the films was witnessed by capturing the photographs of the plates in a Nikon Coolpix camera and analyzed visually.[15]

5.2.3. Preparation of SRGO nanohybrid

To prepare the nanohybrid, 64 mg of $Na_2S_2O_3$ was dissolved in 50 mL millipore water to make a thiosulfate solution. Then 35 mg GO was added to the solution, which was ultrasonicated for 1 h to yield a GO dispersed thiosulfate solution. Then 10 mL of *C. limon* juice was added into the solution, wherein sodium thiosulphate underwent a disproportionation reaction to form sulfur and sulfur dioxide in the acidic environment. After the reactants were mixed, 30 min of equilibrium time was allowed for the completion of the reaction. After equilibration, the sample was ultrasonicated in a bath for 5 min. The resulting suspension was washed by repeated centrifugation with millipore water and acetone. Then it was dried in a vacuum oven at 40 °C.

5.2.4. Preparation of HPU/SRGO nanocomposite

HPU/SRGO nanocomposite was prepared following the same method as it was used to prepare HPU/RGO nanocomposite in the sub-chapter 3C, section 3C.2.4. Only required amount of dispersed SRGO nanohybrid in DMAc (0.5, 1 and 2 wt% with respect to total weight of nanocomposite, separately) was incorporated instead of RGO in 1st step of the polymerization reaction to obtain *in situ* HPU/SRGO nanocomposite. The nanocomposites with 0.5, 1 and 2 wt% of SRGO nanohybrid were encoded as HPU/SRGO0.5, HPU/SRGO1, and HPU/SRGO2, respectively.

5.3. Results and discussion

5.3.1. Preparation of SRGO nanohybrid

In this single-step preparation of SRGO nanohybrid, sodium thiosulfate solution and GO aqueous dispersion were mixed well before addition of lemon juice. The basic sodium thiosulfate can undergo a redox reaction with GO to form a slightly more graphitic carbon than GO and initiate the formation of sulfur nanoparticles.[16] These nucleating sites grow further to form sulfur nanoparticles by disproportionation reaction of the remaining thiosulfate. As lemon juice mainly contains citric and ascorbic acids, which are responsible for the formation of sulfur nanoparticles through a disproportionation reaction, as shown in first part of **Scheme 5.1** (inset). The plausible mechanisms of the simultaneous reduction of

GO and formation of sulfur nanoparticles are shown in **Scheme 5.1**. During the disproportionation reaction of thiosulfate, sulfur dioxide (SO_2) was formed along with sulfur nanoparticles. This SO_2 transforms to HSO_3^- and H^+ in the aqueous medium. The generated H^+ helps to further the disproportionation reaction of thiosulfate and HSO_3^- helps to reduce the GO sheet by following the deoxygenation mechanism as shown in path 1 of **Scheme 5.1**. During this reduction, HSO_3^- is oxidized to SO_3 (as shown in **Scheme 5.1**), which formed sulfuric acid by reaction with water.[17] The H^+ generated from H_2SO_4 further helps to advance the above disproportionation reaction. The reduction of GO is also accompanied by the polyphenolic compounds of lemon juice and the conjugated base of ascorbic acid, as shown in path 2 of **Scheme 5.1**.[18] As all of the above-mentioned reactions were occurring simultaneously, the overall time for the formation of SRGO nanohybrid was minimal (30 min).

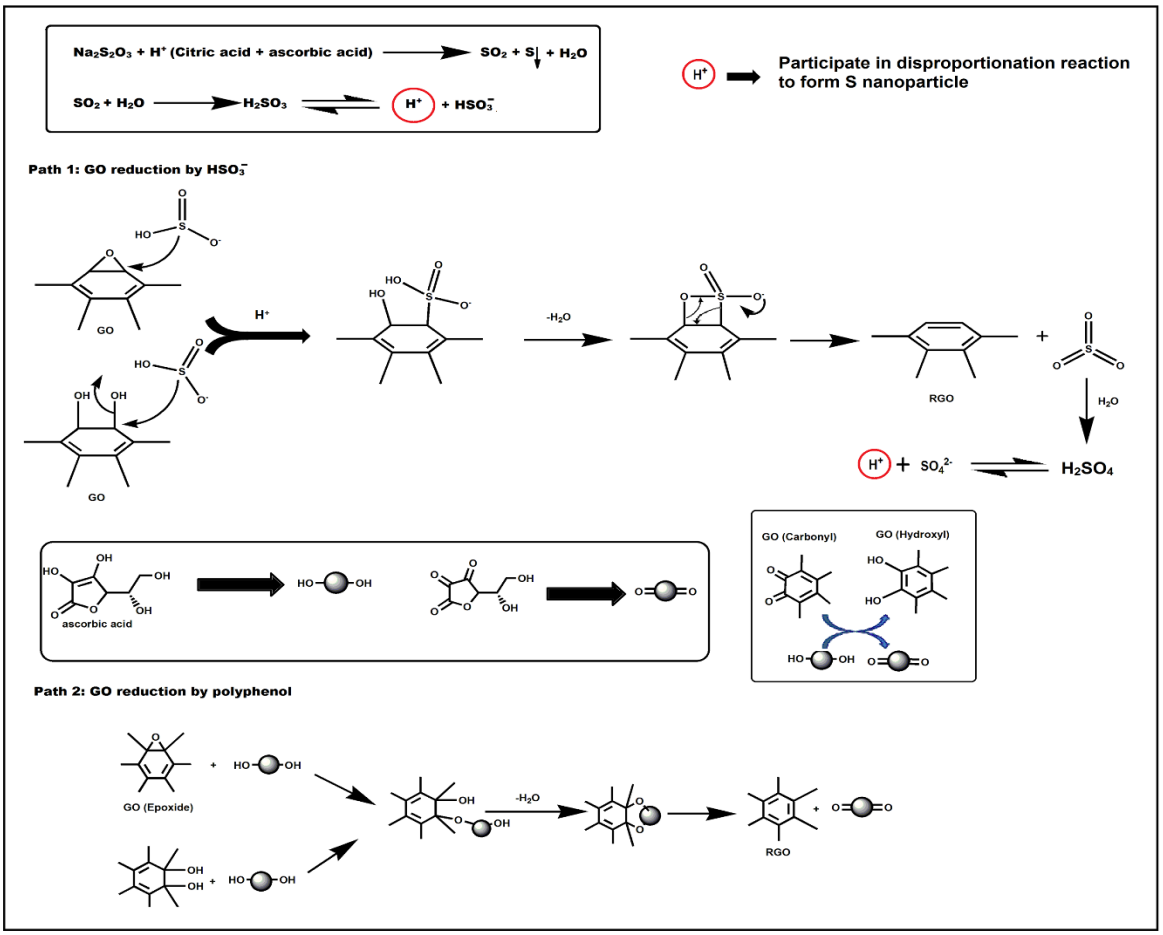

Scheme 5.1 Plausible mechanism of simultaneous reduction of GO and formation of sulfur nanoparticles

5.3.2. Characterization of SRGO nanohybrid

FTIR spectra of GO and SRGO nanohybrid are shown in **Figure 5.1**. In the spectrum of SRGO nanohybrid, the absence of a carbonyl band at 1720 cm^{-1} clearly indicated deoxygenation of the group.[19,20] Also in the spectrum of SRGO nanohybrid, C–H band stretching was found at 2919 and 2842 cm^{-1}, which suggested that some polyphenolic compounds are present in the surface of nanohybrids.[21] In addition to that weak evidence of the existence of C–O–C bonds at about 1200 cm^{-1} in the SRGO nanohybrid was also noticed, which may be due to the presence of some polyphenolic compounds or partially existence with C–O bonds at the edges of SRGO nanohybrid even after the reduction.[21]

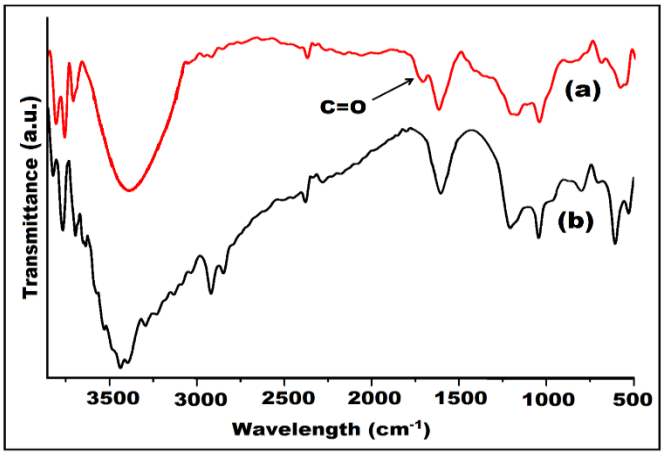

Figure 5.1 FTIR spectra of (a) GO and (b) SRGO nanohybrid [spectra of GO is used from sub-chapter 3A for better comparison]

Raman spectra of GO and SRGO nanohybrid were taken to evaluate the nature of the carbon and sulfur in them (**Figure 5.2**). In the spectrum of GO, the characteristic bands were found at 1322 and 1584 cm^{-1} for the D and G bands, respectively.[21] After the reduction of GO, the intensity ratio of D-band to G-band (I_D/I_G) increased from 0.88 to 1.12 in the spectrum of SRGO nanohybrid. The presence of characteristic band due to the A_1 symmetry mode of the sulfur–sulfur bond at 520 cm^{-1} and the increase of the I_D/I_G ratio in SRGO nanohybrid clearly indicated the decoration of sulfur nanoparticles on RGO sheets and the extent of reduction, respectively.[22]

The XRD patterns of GO, sulfur nanoparticles and SRGO nanohybrid are shown in **Figure 5.3**. In the diffraction pattern of the sulfur nanoparticles, the presence of peaks at 2θ = 23°, 25.8°, 27.7° and 31.39° for the (111), (004), (103) and (113) planes, respectively, clearly reflected that the sulfur nanoparticles were in anorthic form (JCPDS#89–6764). It is

noteworthy to mention that no peak for GO or RGO appeared in the diffraction pattern of SRGO nanohybrid, which proves that the graphene sheets are in a substantially exfoliated state and do not restack upon the decoration of sulfur nanoparticles.[10] Therefore, in the diffraction pattern of SRGO nanohybrid, peaks for sulfur nanoparticles were only found. Further, the amount of sulfur is sufficiently high, which may decorate the surface of RGO almost completely.[12]

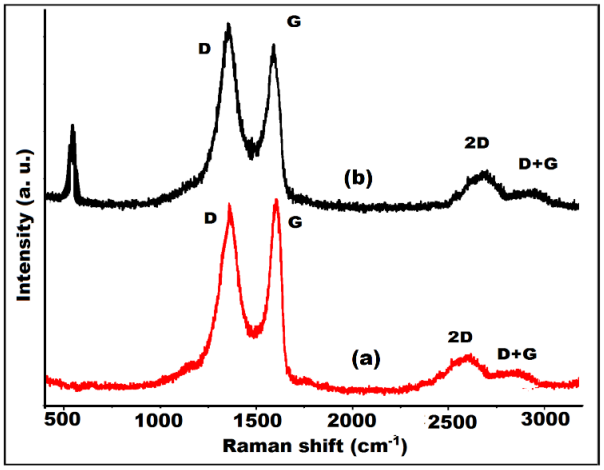

Figure 5.2 Raman spectra of (a) GO and (b) SRGO nanohybrid [spectra of GO is used from sub-chapter 3A for better comparison]

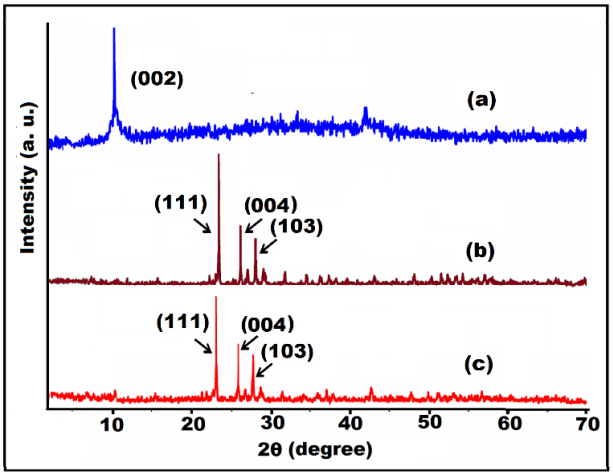

Figure 5.3 XRD patterns of (a) GO, (b) sulfur nanoparticles and (c) SRGO nanohybrid [XRD patterns of GO is used from sub-chapter 3A for better comparison]

TGA thermograms of GO and SRGO nanohybrid are shown in **Figure 5.4**. In the thermogram of SRGO nanohybrid, an almost similar two-step degradation like GO was

observed. But in the first step, the maximum degradation occurred at around 200–240 °C due to the loss of sulfur and some remaining oxygenated groups.[23]

The morphology of SRGO nanohybrid was inspected by HRTEM study. From the HRTEM micrograph, it is clearly revealed that sulfur nanoparticles (average particle size, 23 nm) are uniformly distributed on the surface of RGO sheets (**Figure 5.5**a). The SAED pattern indicated that the sulfur nanoparticles are semi-crystalline in nature (inset of **Figure 5.5**a). The crystal lattice fringes with d-spacing of 0.28 nm can be assigned to the (113) plane of the sulfur nanoparticles, which is consistent with the XRD results (**Figure 5.5**b).

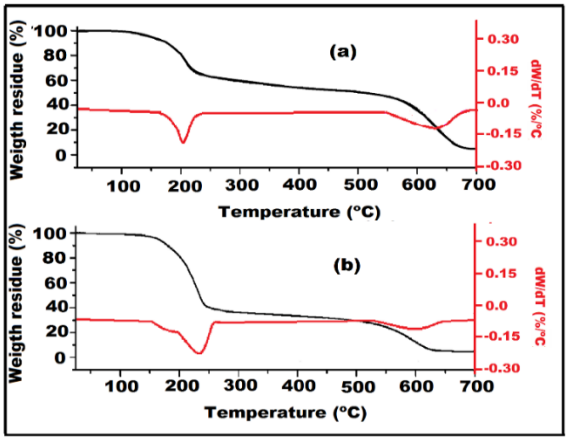

Figure 5.4 TGA (black lines) thermograms and DTG (red lines) curves of (a) GO and (b) SRGO nanohybrid [thermogram of GO is used from sub-chapter 3A for better comparison]

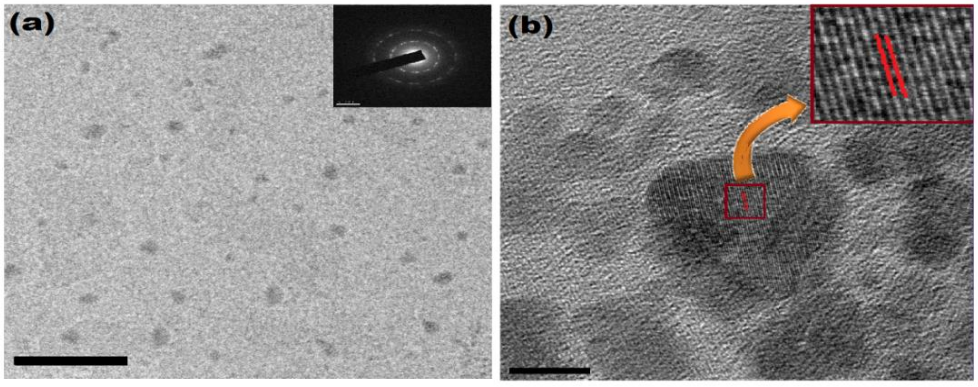

Figure 5.5 TEM images (a) at low magnification (scale bar = 200 nm) showing sulfur nanoparticles distribution and inset shows semi crystalline SAED patterns of SRGO nanohybrid and (b) at high magnification (scale bar = 10 nm) showing the presence of the lattice planes and distance of lattice plane is 28 nm (shown by red line in the inset)

5.3.3. Characterization of HPU/SRGO nanocomposite

FTIR spectra of HPU/SRGO nanocomposites are shown in **Figure 5.6**. The formation of urethane linkages in the nanocomposite was confirmed by the presence of characteristic bands as mentioned in Chapter 2, section 2.3.2. The increase in broadening of the –OH band and shifting of the C=O band from 1700 to 1690 cm^{-1} were observed with the increase in the amount of SRGO nanohybrid in the nanocomposite similar to others studied nanocomposites. This indicated the presence of interactions among polymer chains and SRGO nanohybrid, which are increased with the nanohybrid content.[24]

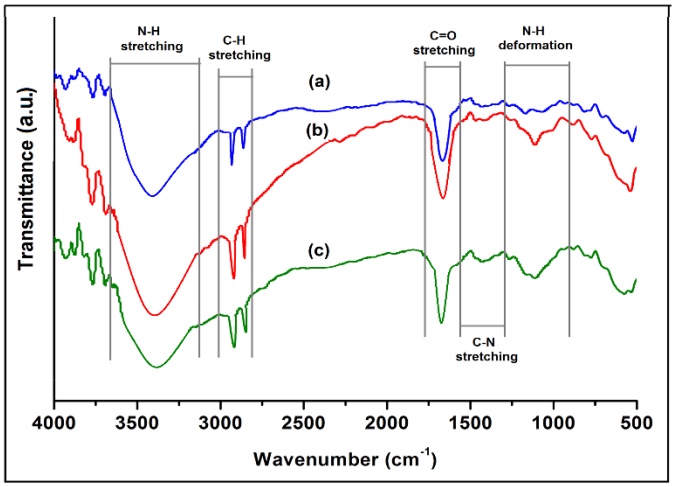

Figure 5.6 FTIR spectra of (a) HPU/SRGO0.5, (b) HPU/SRGO1 and (c) HPU/SRGO2

In the XRD patterns of HPU/SRGO nanocomposites, two distinct peaks at 2θ =21.1 and 23.4 are observed in **Figure 5.7** for the crystals of PCL moiety similar to pristine HPU as stated in Chapter 2, section 2.3.2. In the nanocomposites, minor shifting of PCL peaks towards a higher angle was noticed, due to the formation of a dense structure compared to pristine HPU.[25] A slight increase in the peak intensity of the PCL moiety was also observed with increased in the amount of the nanohybrid due to the nucleating effect of it. Importantly, distinct peaks for the nanohybrid are not observed in the XRD patterns of nanocomposites because a small amount of SRGO nanohybrid was used to fabricate the nanocomposite.[24]

5.3.4. Mechanical properties of HPU/SRGO nanocomposite

The stress–strain profiles of HPU/SRGO nanocomposites are shown in **Figure 5.8**. The nanocomposite demonstrated extensive enhancement in mechanical properties after the incorporation of a small amount of SRGO nanohybrid compare to pristine HPU (Table 2.3,

Chapter 2). Mechanical properties, such as tensile strength, tensile modulus, elongation at break and toughness, are summarized in **Table 5.1**. The presence of strong interfacial interactions provided efficient load transferability between the nanohybrid and the polymer matrix.[26] This resulted in the outstanding mechanical properties of the nanocomposite. Moreover, due to the formation of the covalent bonds between prepolymer chains and functional groups of nanohybrid, hard segments of the HPU chains become stiff similar to HPU/RGO nanocomposite (sub-chapter 3C, section 3C.3.4), resulting in high modulus and strength.[27] All the nanocomposites exhibited dose-dependent mechanical properties. HPU/SRGO0.5 nanocomposite demonstrated typical elastomeric stress–strain profile like pristine HPU, whereas HPU/SRGO1 and HPU/SRGO2 demonstrated typical flexible plastic stress–strain profile.

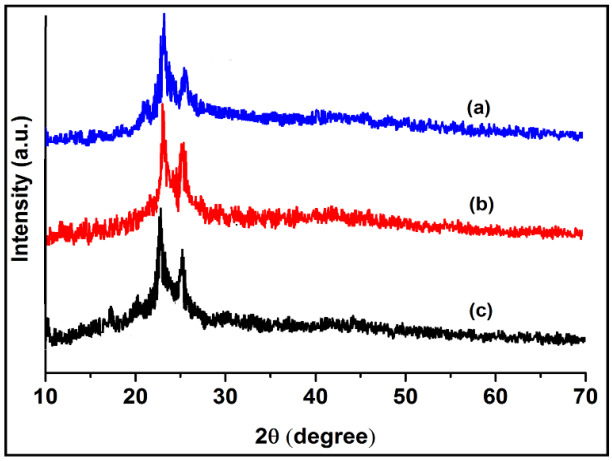

Figure 5.7 XRD patterns of (a) HPU/SRGO0.5, (b) HPU/SRGO1 and (c) HPU/SRGO2

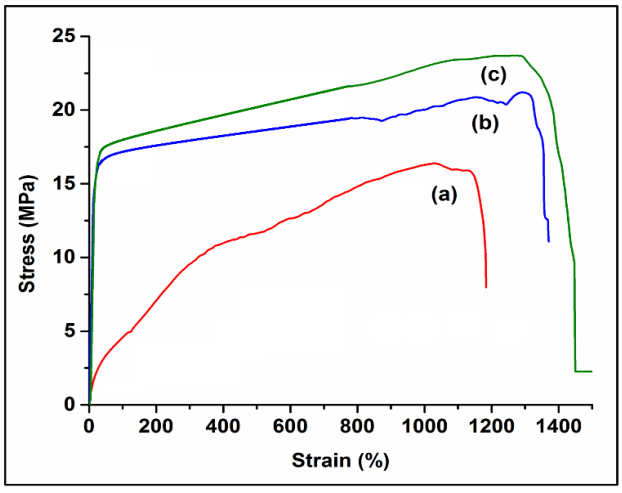

Figure 5.8 Stress–strain profiles of (a) HPU/SRGO0.5, (b) HPU/SRGO1 and (c) HPU/SRGO2

From **Figure 5.8**, it is also clear that the tensile modulus and strength of nanocomposite are enormously enhanced in HPU/SRGO1 and HPU/SRGO2 nanocomposites, compared with HPU/SRGO0.5 nanocomposite. This indicated that a small amount of nanohybrid (0.5 wt%) does not establish appropriate interfaces, and hence there might be a lack of load transfer from the polymer matrix to the nanohybrid. This is directly reflected in the low improvement in the mechanical properties of HPU/SRGO0.5 nanocomposite. Toughness of the nanocomposite was also enhanced by higher amount of nanohybrid, and all the nanocomposite demonstrated excellent toughness compared with pristine HPU (Table 2.3, Chapter 2). Similar to HPU/RGO nanocomposite, HPU/SRGO nanocomposite also exhibited a higher elongation at break compared to pristine HPU, and it was found to increase with increasing nanohybrid content. The enhancement of elongation at break is due to the alignment of polymer chains along the loading direction during the initial stress and sliding of layers of RGO at high stress as mentioned in sub-chapter 3C, section 3C.3.4.[27] The elasto-plastic behavior of graphene sheets may also be another reason for this observation.[28]

Table 5.1 Mechanical properties of HPU/SRGO nanocomposite

Nanocomposite	Tensile strength (MPa)	Tensile modulus (MPa)	Elongation at break (%)	Toughness (MJm^{-3})
HPU/SRGO0.5	16.5 ± 0.7	13.6 ± 0.5	1186 ± 35	138.2 ± 2.2
HPU/SRGO1	21.6 ± 1.1	130.64 ± 1.2	1372 ± 30	268.9 ± 3.4
HPU/SRGO2	24.3 ± 1.3	137.74 ± 2.2	1456 ± 45	313.5 ± 4.3

5.3.5. Thermal properties of HPU/SRGO nanocomposite

Thermal behaviors of the prepared nanocomposites were evaluated by TGA and the thermograms are shown in **Figure 5.9**. HPU/SRGO nanocomposite shows almost similar thermograms but the nanocomposites demonstrate higher thermal stability compared to the pristine HPU (Chapter 2, section 2.3.8). From the thermograms, initial degradation temperature ($T_{initial}$) and midpoint degradation temperature (50% weight loss) are calculated and summarized in **Table 5.2**. The improvement in thermal stability of the nanocomposite may be attributed to the so-called "tortuous path" effect of RGO, which delays the escape of volatile degradation products and restricts the movement of polymeric chains due to the presence of strong interfacial interactions between HPU and the nanohybrid.[29]

The degree of crystallinity and T_m of the prepared nanocomposite were evaluated by DSC analysis (**Figure 5.10**). The crystallinity found in the nanocomposite is due to the presence of a crystalline PCL moiety in the soft segment of HPU as mentioned in Chapter 2, section 2.3.8. The dose-dependent degree of crystallinity and T_m values were observed for the nanocomposite with the content of nanohybrid (**Table 5.2**). These results are due to the fact that the nanohybrid may help to orient the HPU chains in a particular direction and thereby restricting the mobility of the polymeric chains.

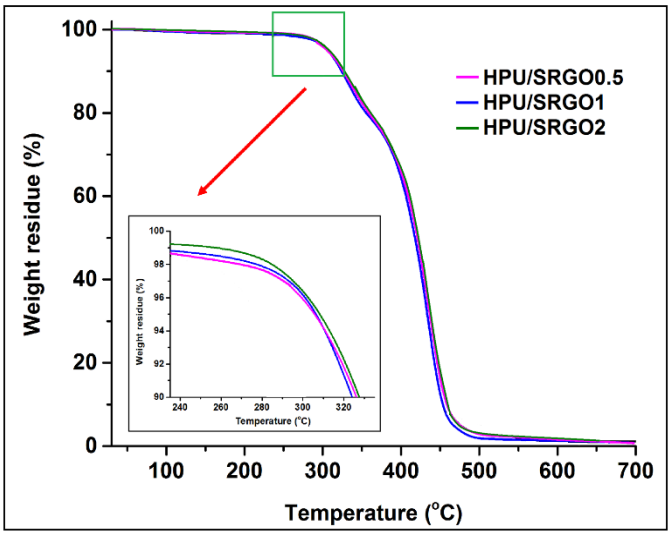

Figure 5.9 TGA thermograms of HPU/SRGO nanocomposite

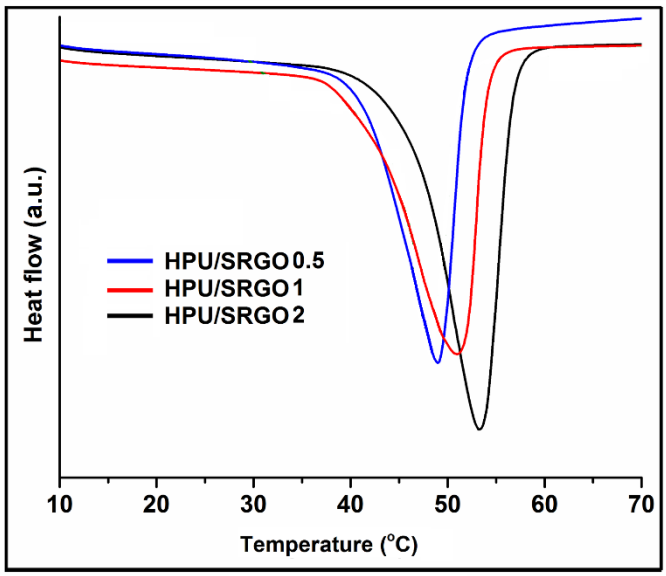

Figure 5.10 DSC curves of HPU/SRGO nanocomposite

Table 5.2 Thermal properties of HPU/SRGO nanocomposite

Nanocomposite	$T_{initial}$ (°C)	Midpoint degradation temperature (°C)	T_m (°C)	Crystallinity (%)
HPU/SRGO0.5	305.48	417.85	49.06	33.15
HPU/SRGO1	306.71	420.39	51.12	35.14
HPU/SRGO2	308.75	421.23	53.29	37.25

5.3.6. Shape memory behavior of HPU/SRGO nanocomposite

Shape memory behavior of HPU/SRGO nanocomposites under sunlight is shown in **Figure 5.11**. All the nanocomposites demonstrated excellent shape fixity and recovery under exposure to MW and sunlight. Shape recovery of the nanocomposite was faster and more efficient upon exposure to MW compared to sunlight. This may be due to excellent MW absorbing capacity of RGO as compared to that of sunlight as mentioned in sub-chapter 3C, section 3C.3.7. Shape recovery time and ratio under different stimuli are tabulated in **Table 5.3**.

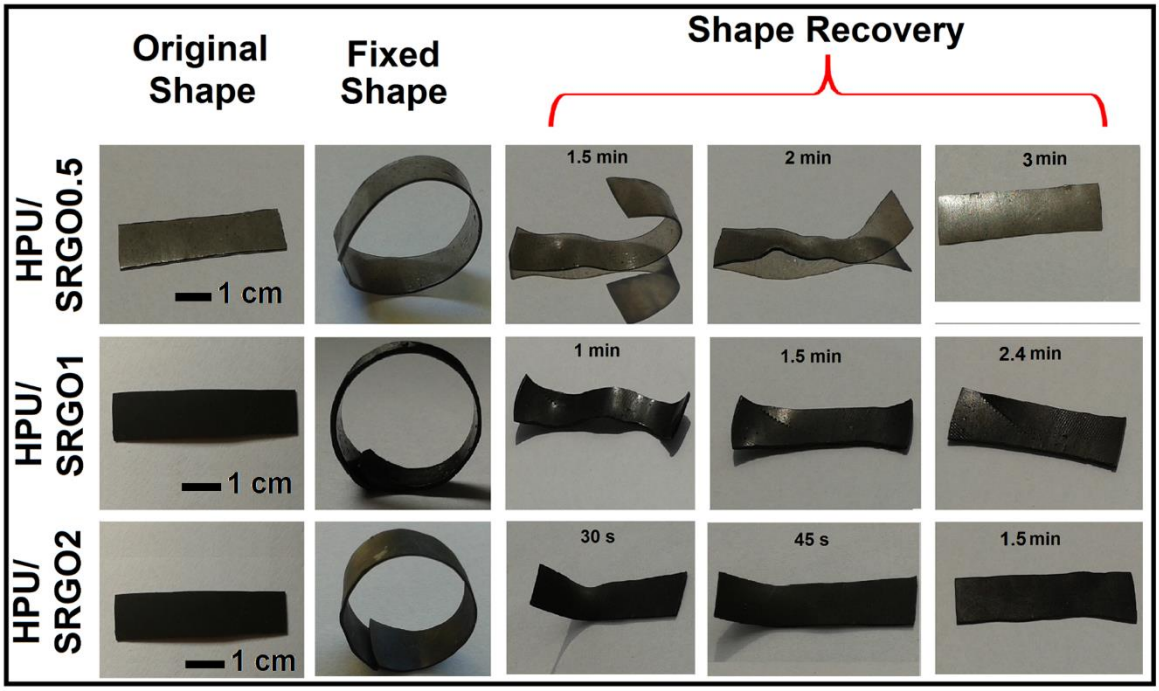

Figure 5.11 Shape-memory behavior of HPU/SRGO nanocomposite under direct sunlight

Table 5.3 Shape memory behavior of HPU/SRGO nanocomposite

Stimulus	HPU/SRGO0.5		HPU/SRGO1		HPU/SRGO2	
	Shape recovery time (min)	Shape recovery (%)	Shape recovery time (min)	Shape recovery (%)	Shape recovery time (min)	Shape recovery (%)
MW	1.16 ± 0.3	96.8 ± 0.1	1.0 ± 0.3	97.6 ± 0.2	0.75 ± 0.3	98.6 ± 0.1
Sunlight	3.0 ± 0.2	96.2 ± 0.1	2.4 ± 0. 3	97.4 ± 0.2	1.5± 0.1	98.5 ± 0.1

The nanocomposite exhibited better shape recovery compared to HPU. Due to the homogenous distribution of SRGO nanohybrid in the HPU matrix, high stored elastic strain energy is generated in the nanocomposite, which helps the nanocomposites to achieve high recovery stress by releasing the stored elastic strain energy.[30] The shape recovery also found to be increased with increase in loading of nanohybrid. More unlocked oriented chains are generated owing to increase in crystallinity of the nanocomposite on an incorporation of nanohybrid (as obtained from DSC and XRD results). These unlocked chains can produce an instantaneous retractive force upon elimination of the load because of the elastic entropy, and hence it improved the shape recovery.

5.3.7. Self-healing properties of HPU/SRGO nanocomposite

Tensile tests and optical images were used to examine the self-healing behavior of HPU/SRGO nanocomposite similar to HPU/IO-RGO nanocomposite (Chapter 4, section 4.3.8). Fracture of the nanocomposite is effectively healed by exposure of direct sunlight and MW. The healing efficiency of nanocomposite under sunlight and MW are also shown in **Figure 5.12**. The healing efficiency of HPU/SRGO nanocomposite also depends on loading of SRGO nanohybrid, power input of MW and exposure time similar to HPU/IO-RGO nanocomposite as shown in **Figure 5.13**. All the nanocomposites were effectively healed within 50–60 s under MW power (540 W) and within 7.5–10 min under direct sunlight. Even though, HPU/SRGO nanocomposite takes more time to heal the crack compare to HPU/IO-RGO nanocomposite. This is due to high MW and sunlight absorbing capacity of IO-RGO nanohybrid than SRGO nanohybrid as IO nanoparticles also possesses good MW absorption ability and thermal conductivity, whereas sulfur nanoparticles are unable to absorb such energy.[31] During the healing process, SRGO nanohybrid absorbed energy from the stimulus, and then transferred this energy to the HPU matrix. The soft

segment of HPU became soften by gaining the energy. Thus, the crack could repair with a higher mobility of the soft segment of HPU. At the same time, the hard segment of HPU helps to retain its original shape. The shape memory properties of nanocomposite also played a vital role in the healing process as mentioned in previous chapter, section 4.3.8. When energy is transferred to HPU chains by SRGO nanohybrid, it was activated, and then the internal stress was released. Therefore, the notched surface of the crack was first healed with the help of the recovery force from the bottom before complete repairing of the crack.[32] In this work, self-healing was achieved by the rearrangement of soft segments of HPU with the assistance of the shape memory effect similar to HPU/IO-RGO nanocomposite, thus the healing of the prepared nanocomposite could be repeated again and again. Therefore, the healing ability of the nanocomposite remains almost same even after the fifth cycle of the experiment under both sunlight and MW (**Figure 5.12**).

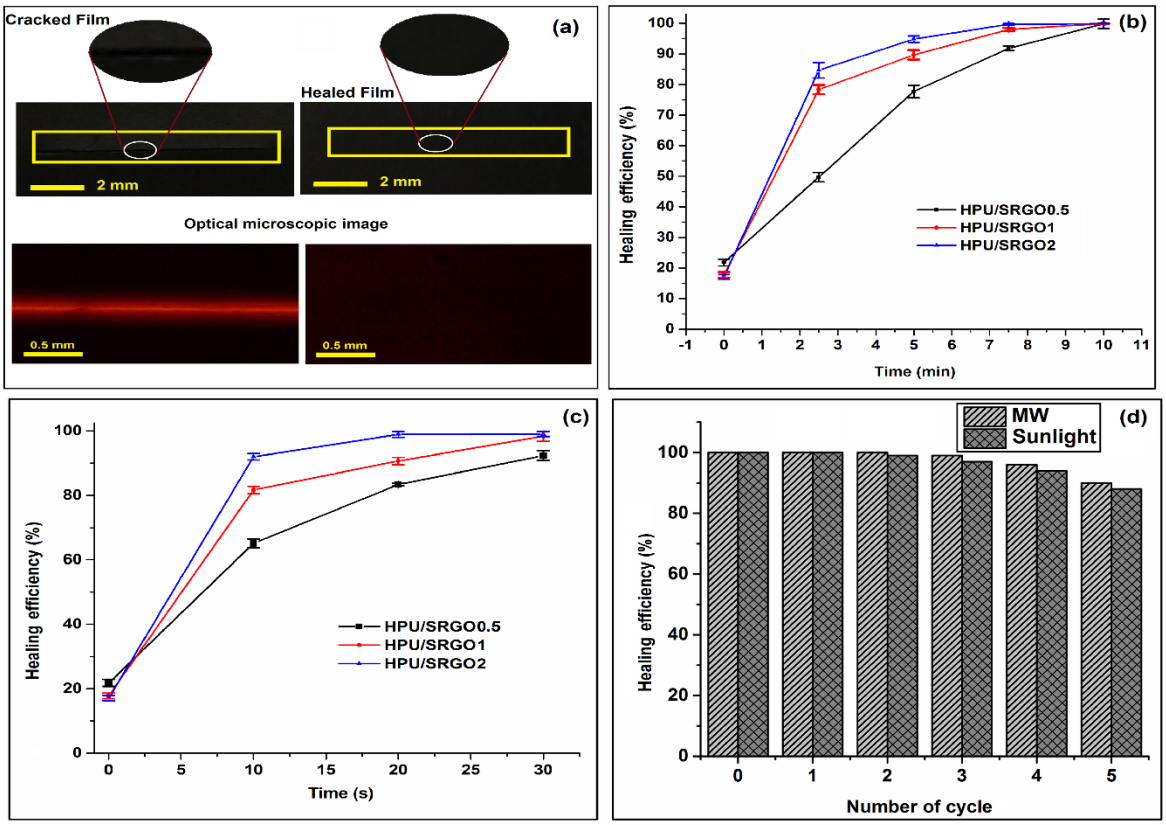

Figure 5.12 (a) Digital and optical microscopic photographs of cracked and healed nanocomposite films; healing efficiency of the nanocomposite under (b) sunlight and (c) MW (360 W); and (d) repeatable healing efficiency of the nanocomposite under sunlight and MW

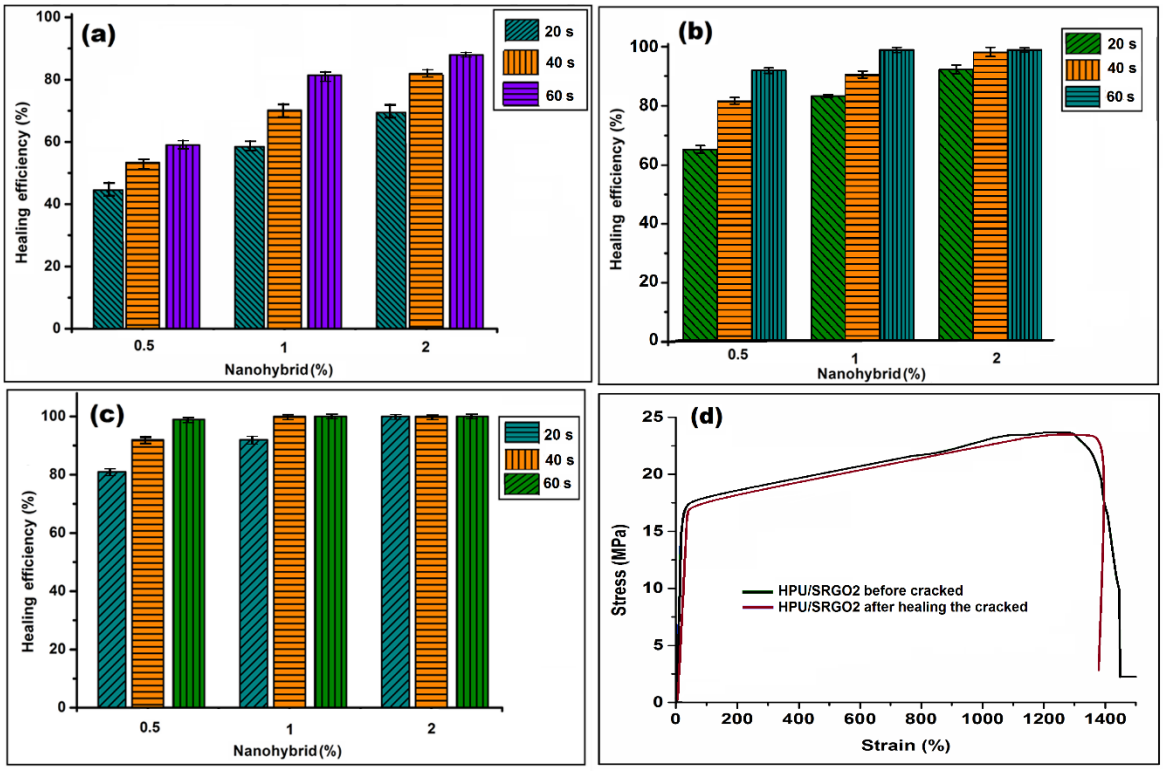

Figure 5.13 The healing efficiency of the nanocomposite at different MW power input of (a) 180 W, (b) 360 W and (c) 540 W; and (d) representative stress–strain curves of HPU/SRGO2 before cracked and after healing the cracked

5.3.8. Antimicrobial activity of HPU/SRGO nanocomposite

SRGO nanohybrid exhibited the lowest MIC against both bacteria and fungus (**Table 5.4**). As sulfur nanoparticles and RGO showed a strong antimicrobial effect, the nanohybrid demonstrates a synergistic effect against the tested microbes. However, indirect contact of SRGO nanohybrid with the microbial strains suppressed the inhibitory action in case of the nanocomposite. Thus, a high dose of the nanocomposite was required to show the inhibitory effect. MIC values suggest that the nanocomposite can inhibit both gram positive and gram negative bacteria, though the effect is more pronounced for the former. Contrarily, pristine HPU exhibited an inhibitory effect at a very high dose, which implies that SRGO nanohybrid is mainly responsible for conferring antimicrobial efficacy to the nanocomposites. Antifungal activity of the nanohybrid, as well as nanocomposite, was also found to be significantly effective. However, in each case, the reduction of growth was observed when incubated with HPU/SRGO2 nanocomposite films. Statistical measurements (Two-way ANOVA) revealed that the MIC values were significantly different from each other, with least significant difference (LSD) 0.63 and $p < 0.05$. It is clearly visible from **Figure 5.14**(a–

c) that microbial growth exponentially increased with time in the controls. On the other hand, the presence of HPU/SRGO2 nanocomposite inhibited the growth rate of each microbe, considered under the test. Another, interesting inference derived from the assay is that the growth rate of the strains is not considerably hampered by the presence of HPU. This again validates the efficient antimicrobial activity of SRGO nanohybrid. Microorganisms adhered to the antimicrobial surfaces lost their morphological integrity.[33] Cell membrane lysis is the vital factor for the decrement in growth rate. To ascertain this, *E. coli* was considered as a representative microbe for SEM analysis. From **Figure 5.14**(d–f) it is observed that membrane disruption occurred in the bacterial cells that attached to HPU/SRGO2 surface. Red marks indicate the irregularity in the cellular structures and agglomeration of the dead cells. However, bacteria attached to HPU surface did not lose their cellular structure. This confirmed the microbial growth-resisting potential of HPU/SRGO2 nanocomposite. This antimicrobial property is very useful for the fabrication of various advanced materials that could prevent microbial contamination and infections.

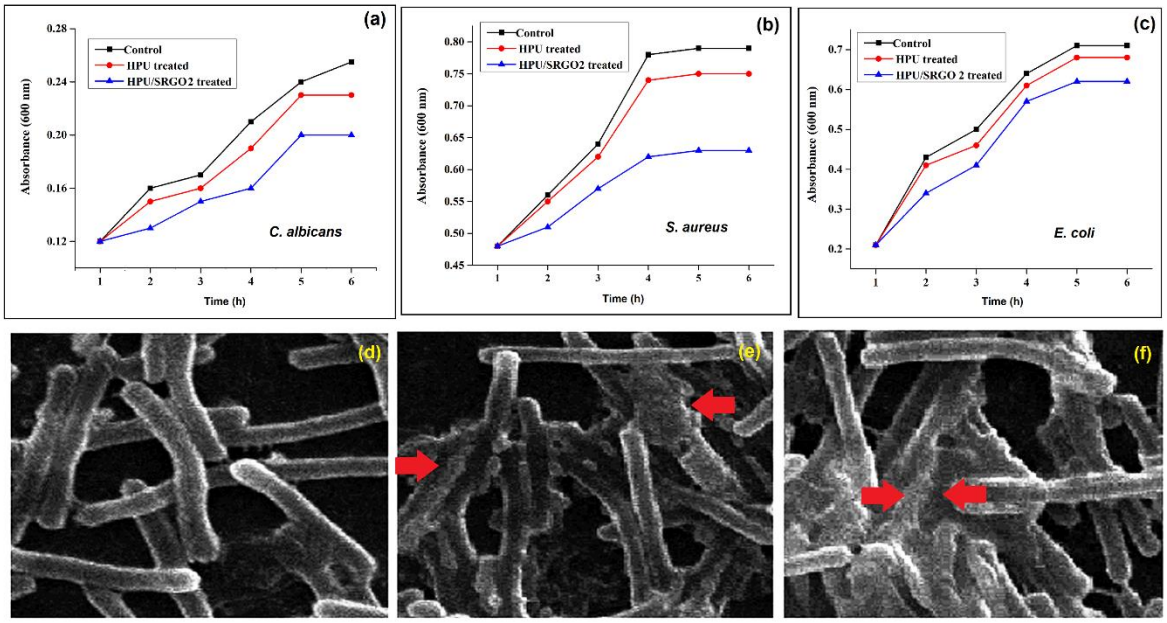

Figure 5.14 Inhibition of growth of (a) *C. albicans*, (b) *E. coli*, (c) *S. aureus* against HPU and HPU/SRGO2; and SEM images of *E. coli* cells adhered to (d) HPU, (e) HPU/RGO2 and (f) HPU/SRGO2

Another assay was performed to verify the possibility of microbial growth, in the proximity of HPU and HPU/SRGO2 nanocomposite. Thus, images were taken and analyzed for the films, laid in Petri plates with each of the test microorganisms (**Figure 5.15**). Images

confirmed that none of the microbes could grow over the HPU/SRGO2 nanocomposite surface within an area of 1.5 cm^2, whereas significant growth was witnessed over the surface of HPU. This indicated that the nanocomposite did not allow microbial fouling over its surface, even in close contact with the microbes. The overall study endorses the material as an advanced antimicrobial nanocomposite with high mechanical attributes.

Table 5.4 MIC against bacteria and fungus

Microbe	HPU (μg/ml)	RGO (μg/ml)	Sulfur nanoparticles (μg/ml)	SRGO (μg/ml)	HPU/SRGO2 (μg/ml)
S. aureus	180 ± 2.6	22.7 ± 1.57	18.3 ± 0.57	13.7 ± 1.50	33.7 ± 1.52
E. coli	245 ± 3.2	31.0 ± 1.00	21.7 ± 1.52	19.3 ± 0.57	43.0 ± 2.00
C. albicans	272 ± 3.6	47.0 ± 1.00	33.7 ± 1.50	29.0 ± 1.00	63.3 ± 1.52

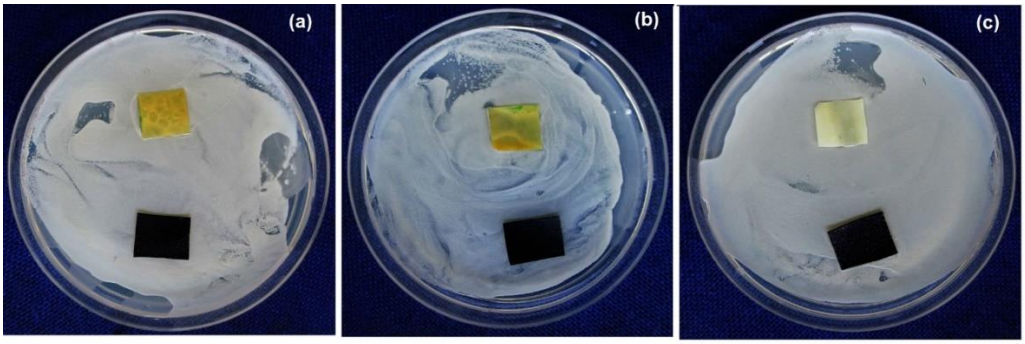

Figure 5.15 Growth images of (a) *S. aureus*, (b) *E. coli* and (c) *C. albicans* in close proximity of HPU and HPU/SRGO2

5.4. Conclusion

So in this study, a greener one-step strategy is developed to prepare SRGO nanohybrid using *C. limon* juice. Also, a tough HPU/SRGO nanocomposite was fabricated by using the prepared nanohybrid. The fabricated nanocomposite exhibited improved mechanical and thermal properties after incorporation of a small amount of nanohybrid owing to the good interaction between nanohybrid and HPU. The nanocomposite also showed excellent rapid and repeatable self-healing and shape recovery by MW and sunlight. The presence of SRGO nanohybrid in nanocomposite provided good antimicrobial activity against gram positive and negative bacteria along with fungus. Thus, the multifunctional smart nanocomposite shows a great potential in the domain of advanced material.

References

1. Gu, J.D. Microbiological deterioration and degradation of synthetic polymeric materials: Recent research advances, *Int. Biodeterior. Biodegrad.* **52** (2), 69--91, 2003.
2. Kalita, H., et al. Biodegradable solvent-induced shape-memory hyperbranched polyurethane, *J. Polym. Res.* **19**, 9982 (pp 6), 2012.
3. Yahia, L. *Shape Memory Polymers for Biomedical Applications*, Woodhead Publishing, Cambridge, 2015.
4. Kenawy, E.R., et al. The Chemistry and applications of antimicrobial polymers: a state-of-the-art review, *Biomacromolecules* **8** (5), 1359--1384, 2007.
5. Tobaldi, D.M., et al. Silver-modified nano-titania as an antibacterial agent and photocatalyst, *J. Phys. Chem. C* **118** (9), 4751--4766, 2014.
6. Marambio-Jones, C., & Hoek, E.M.V. A review of the antibacterial effects of silver nanomaterials and potential implications for human health and the environment, *J. Nanopart. Res.* **12** (5), 1531--1551, 2010.
7. Liu, S., et al. Antibacterial activity of graphite, graphite oxide, graphene oxide, and reduced graphene oxide: Membrane and oxidative stress, *ACS Nano* **5** (9), 6971--6980, 2011.
8. Chen, J., et al. Graphene oxide exhibits broad-spectrum antimicrobial activity against bacterial phytopathogens and fungal conidia by intertwining and membrane perturbation, *Nanoscale* **6**, 1879--1889, 2014.
9. Schneider, T., et al. Selective antimicrobial activity associated with sulfur nanoparticles, *J. Biomed. Nanotechnol.* **7** (3), 395--405, 2011.
10. Park, M., et al. One-pot synthesis of a sulfur-impregnated graphene cathode for lithium–sulfur batteries, *Phys. Chem. Chem. Phys.* **14**, 6796--6804, 2012.
11. Zhang, F., et al. Facile and effective synthesis of reduced graphene oxide encapsulated sulfur via oil/water system for high performance lithium sulfur cells, *J. Mater. Chem.* **22**, 11452--11454, 2012.
12. Wang, J., et al. Sulfur-graphene composite for rechargeable lithium batteries, *J. Power Sources* **196**, 7030--7034, 2011.
13. Chaudhuri, R.G., & Paria, S. Synthesis of sulfur nanoparticles in aqueous surfactant solutions, *J. Colloid Interface Sci.* **343**, 439--446, 2010.
14. Penniston, K.L., et al. Quantitative assessment of citric acid in lemon juice, lime juice, and commercially-available fruit juice products, *J. Endourol.* **22**, 567--570, 2008.

15. Barua, S., et al. Biocompatible hyperbranched epoxy/silver–reduced graphene oxide–curcumin nanocomposite as an advanced antimicrobial material, *RSC Adv.* **4**, 47797--47805, 2014.
16. Evers, S., & Nazar, L.F. Graphene-enveloped sulfur in a one pot reaction: a cathode with good coulombic efficiency and high practical sulfur content, *Chem. Commun.* **48**, 1233--1235, 2012.
17. Chen, W., et al. Chemical reduction of graphene oxide to graphene by sulfur-containing compounds, *J. Phys. Chem. C* **114**, 19885--19890, 2010.
18. Fernandez-Merino, M.J., et al. Vitamin C is an ideal substitute for hydrazine in the reduction of graphene oxide suspensions, *J. Phys. Chem. C* **114** (14), 6426--6432, 2010.
19. Si, Y., & Samulski, E.T. Synthesis of water soluble graphene, *Nano Lett.* **8**, 1679--1682, 2008.
20. Wang, Y., et al. Facile synthesis of soluble graphene via a green reduction of graphene oxide in tea solution and its biocomposites, *ACS Appl. Mater. Interfaces* **3**, 1127--1133, 2011.
21. Kuila, T., et al. A green approach for the reduction of graphene oxide by wild carrot root, *Carbon* **50** (3), 914--921, 2010.
22. Guo, J., et al. Sulfur-impregnated disordered carbon nanotubes cathode for lithium sulfur batteries, *Nano Lett.* **11**, 4288--4294, 2011.
23. Cao, Y., et al. Sandwich-type functionalized graphene sheet-sulfur nanocomposite for rechargeable lithium batteries, *Phys. Chem. Chem. Phys.* **13**, 7660--7665, 2011.
24. Kalita, H., & Karak, N. Bio-based hyperbranched polyurethane/multi-walled carbon nanotube nanocomposites as shape memory materials, *Polym. Compos.* **35** (4), 636--643, 2014.
25. Lee, H.F., & Yu, H.H. Study of electroactive shape memory polyurethane–carbon nanotube hybrids, *Soft Matter* **7**, 3801--3807, 2011.
26. Meera, K.M.S., et al. The influence of applied silica nanoparticles on a bio-renewable castor oil based polyurethane nanocomposite and its physicochemical properties, *Phys. Chem. Chem. Phys.* **16**, 9276--9288, 2014.
27. Chen, Z., & Lu, H. Constructing sacrificial bonds and hidden lengths for ductile graphene/polyurethane elastomers with improved strength and toughness, *J. Mater. Chem*. **22**, 12479--12490, 2012.

28. Yoo, H.J., et al. High-speed actuation and mechanical properties of graphene-incorporated shape memory polyurethane nanofibers, *J. Phys. Chem. C* **118** (19), 10408--10415, 2014.
29. Wang, X., et al. *In situ* polymerization of graphene nanosheets and polyurethane with enhanced mechanical and thermal properties, *J. Mater. Chem.* **21**, 4222--4227, 2011.
30. Deka, H., et al. Biocompatible hyperbranched polyurethane/multi-walled carbon nanotube composites as shape memory materials, *Carbon* **48**, 2013--2022, 2010.
31. Zhao, X., et al. Excellent microwave absorption property of graphene-coated Fe nanocomposites, *Sci. Rep.* **3**, 3421(pp 5), 2013.
32. Bai, Y., et al. Poly(vinyl butyral) based polymer networks with dual-responsive shape memory and self-healing properties, *J. Mater. Chem. A* **2**, 9169--9177, 2014.
33. Knetsch, M.L.W., & Koole, L.H. New strategies in the development of antimicrobial coatings: the example of increasing usage of silver and silver nanoparticles, *Polymers* **3**, 340--366, 2011.